Check for updates

ZnO and reduced graphene oxide electrodes for all-in-one supercapacitor devices

Merve Buldu-Akturk,[†][a] Maryam Toufani,[†][b] Ali Tufani[c] and Emre Erdem ⓘ *[a,d]

Reduced graphene oxide/zinc oxide (rGO/ZnO) hybrid nanocomposites were prepared from synthesized GO and high energy ball milled (HEBM) ZnO for supercapacitor electrodes. Evolution of intrinsic point defects and defect-induced morphological, structural and size-dependent properties of rGO/ZnO hybrid nanocomposites were investigated using electron paramagnetic resonance (EPR) spectroscopy. CV, PEIS and GCPL techniques were employed to investigate the electrochemical behavior of the electrode materials and the effects of defects on the electrochemical performance of the electrodes by using the standard two-electrode cell in a 6 M KOH electrolyte. Analyses of the obtained CV and impedance profiles have shown the pseudocapacitive and EDLC-type contributions in the supercapacitors. Cycling stabilities were evaluated using galvanostatic charge–discharge curves at current densities between 0.10 and 2.40 A g^{-1}. The capacitance retention of all electrodes was found to be 100% after 30 cycles at 0.30 A g^{-1}. The electrochemical analyses revealed that the incorporation of ZnO that is rich in core defects improved the charge transfer performance and ion diffusion of the rGO electrode.

1. Introduction

Graphene, known as "super carbon", is a single atom thick nanosheet of sp^2-bonded carbon atoms packed into a two dimensional (2D) honeycomb lattice.[1] Owing to its extraordinary thermal, mechanical, and electrical properties, graphene has been explored in a wide range of research fields including sensors,[2,3] catalysts,[4,5] supercapacitors[6,7] and batteries.[8] However, researchers reported that the pure graphene produced by chemical-based methods shows moderate electrical conductivity because of the irreversible agglomeration (or restacking) problem due to weak van der Waals interactions between the neighboring graphene sheets after chemical reduction of graphene oxide to graphene.[9–11] Therefore, many efforts have focused on hybridizing graphene with metal/metal oxide nanoparticles to overcome the restacking problem, because there are still many challenges in obtaining stable reduced graphene oxide (rGO) sheets *via* the present reduction methods.[9,11,12]

As one of the most important wide-band gap piezoelectric semiconductors, ZnO has great potential applications in the field of solar cells, photodetectors and UV-light emitters.[13–15] The defective nature of ZnO is an important advantage of this material since some properties of ZnO can be changed or tailored by the existence of intrinsic point defects. Zinc vacancies, zinc on interstitial sites, oxygen on interstitial sites, and oxygen vacancies are conceivable intrinsic defects in ZnO.[16–18] All these defects may act as donor or acceptor levels within the band gaps and most of them can be ionized to become paramagnetic, and thus can be detected by electron paramagnetic resonance (EPR) spectroscopy. Also, it is reported that some hydrogen impurities from air can be absorbed by ZnO and may act as a shallow donor.[19,20] Therefore, controlling the defect structure of the ZnO material during and after synthesis is one of the key parameters to consider.

Most recently, ZnO/graphene nanocomposites have been synthesized and explored owing to their novel properties, such as adsorption performance for removing hazardous heavy metals in wastewater,[21] electrical conductivity,[22] defect related issues,[23,24] and optical transmittance.[22] On combining ZnO and graphene into nanocomposites, graphene behaves as a supporting material for ZnO nanoparticles which anchored on the graphene surface.[25,26] Additionally, the ZnO particles acted as spacers to effectively separate graphene sheets that in turn affected the final performance of the materials composed of rGO.[27] Meanwhile, Cembrero *et al.*[28] reported about a 43% increase in the conductivity of rGO/ZnO hybrid nanomaterials by the coupled chemical and electrochemical reduction

[a]*Faculty of Engineering and Natural Sciences, Sabancı University, 34956 Tuzla, Istanbul, Turkey. E-mail: emre.erdem@sabanciuniv.edu*
[b]*School of Chemistry, National University of Ireland Galway, University Road, H91TK33 Galway, Ireland*
[c]*Department for Materials Synthesis, Jožef Stefan Institute, Jamova 39, SI-1000 Ljubljana, Slovenia*
[d]*Integrated Manufacturing Technologies Research and Application Center & Composite Technologies Center of Excellence, Sabancı University, Teknopark Istanbul, 34906 Pendik, Istanbul, Turkey*
†These authors equally contributed to this work.

method with a 5 mg L^{-1} rGO content in ZnO compared to pure ZnO.

The chemical reduction method to synthesize rGO is the most widely preferred and low-cost method to produce graphene in a large quantity. Besides, hydrazine,[29] ascorbic acid,[30] glucose[31] and ethylene glycol[32] have generally been used in chemical reduction methods as reagents to hybridize graphene with inorganic nanoparticles, such as Ag, Au, SnO$_2$, TiO$_2$, ZnO[25,28,33,34] and polymers.[35,36] Among them, ascorbic acid is a newly reported reducing reagent for GO and inorganic metal/metal–oxide doped GO. This method possesses great advantages due to its soft reduction medium, non-toxicity, environmentally friendly character, non-eroding behavior and inflammability.[37,38] Moreover, many attempts have been made to produce metal nanoparticle (NP) decorated (or attached) graphene by a one-step reduction method using ascorbic acid to control the size of NPs on graphene.[30,39] Surely, one of the best ways to test the electrical performance of the newly introduced materials is to use them as electrode materials in energy storage and harvesting devices, here supercapacitors. Recently, metal oxides have gained attention as promising electrodes in supercapacitors with high electrochemical stability.[40–42]

In this study, high-energy ball milled (HEBM) ZnO nanoparticles milled at two different milling time intervals (15 min and 10 h) were attached onto the surface of graphene oxide (GO), followed by the reduction of the GO/ZnO to rGO/ZnO hybrid nanocomposite by using L-ascorbic acid. Defect induced morphological, structural and size dependent properties of rGO/ZnO were investigated by EPR spectroscopy. Finally, all-in-one supercapacitors were assembled using these hybrid rGO/ZnO nanocomposites as electrodes and their electrochemical performance was tested through electrochemical impedance spectroscopy (EIS), cyclic voltammetry (CV) and galvanostatic cycling with potential limitation (GCPL) techniques.

2. Experimental

2.1 Graphene oxide (GO) preparation

GO was synthesized by a modified Hummers' method.[43,44] Graphite (99.9%, Alfa Aesar) was purchased from Merck, and NaNO$_3$ (Merck) and KMnO$_4$ (99.3%, Pure Chem) were obtained from Grüssing GmbH (Germany). H$_2$SO$_4$ (95–98%) and H$_2$O$_2$ (50%) were obtained from Sigma-Aldrich. In a typical synthesis approach, 1 g of graphite, 46 ml of H$_2$SO$_4$ and 0.5 g of NaNO$_3$ were mixed and stirred at 35 °C for 2 min. Then, the solution was continuously stirred in an ice bath until the temperature reached 0 °C. After that, 3 g of KMnO$_4$ was added gradually and the temperature was not allowed to exceed 20 °C. Subsequently, the solution was held and stirred at 35 °C for 6 h. In an additional step, another 3 g of KMnO$_4$ was added to the solution, and stirred again for 12 h at 35 °C. Finally, 150 ml of H$_2$O containing 10 ml of 50% H$_2$O$_2$ was added slowly while keeping the temperature below 80 °C. As a result,

residual KMnO$_4$ and MnO$_2$ were reduced to Mn^{2+}. The color of the solution changed from dark brown to bright yellow. Firstly, the obtained bright yellow solution was sonicated for 30 min and centrifuged at 4000 rpm for 3 h to collect the product from the solution. Subsequently, 80 ml of 37% HCl was added to the black powder which was dispersed in HCl by stirring for 2 min. By an additional centrifugation step at 4000 rpm for 3 h, the remaining metal ions were removed. Then, the precipitate was washed two times in 150 ml of deionized water, and then 50 ml of absolute ethanol was added and centrifuged at 4000 rpm for 2.5 h to remove acid and Mn^{2+} in the sample. Hence, clean GO was obtained.

2.2 Ball milling of ZnO powder

High energy ball milling (HEBM) is one facile, clean and fast method for changing solid crystals into nano size. This method is generally used for synthesizing semiconductor materials, such as ZnO, magnetic nanomaterials, carbon nanotubes, *etc.* Moreover, it is a safe method without any gas emission through the process.[45] Basically, it is a way to obtain metastable materials and make nanoparticle size distribution more homogeneous.[46] For producing oxides of a metal, ball milling is a good choice since chemical reactions that normally do not take place at room temperature can occur with the high energy ball milling (HEBM) technique.[47] However, HEBM can cause a high extent of deformation in the symmetry structure of particles due to the collisions of the powders and balls during the process. Moreover, the internal stress of particles increases, especially at longer milling times. The high amount of energy that is used during the process is another disadvantage of the process. Commercial (Merck, Germany, grade 99, 99%) high grade ZnO powder was used as the starting material. The commercial powder was milled in a planetary-ball mill (Fritsch Pulverisette 6 classic line) for 15 min and 10 h with a speed of 2100 rpm under atmospheric pressure at room temperature. Seven stainless-steel balls with a diameter of 7 mm and 16 balls with a diameter of 5 mm were used. The ball-to-powder ratio is 6 : 1 by weight approximately. The striking advantage of this technique is that by applying a very low mechanical energy one may reduce the particle size down to a few nanometers.

2.3 Fabrication of a GO/ZnO hybrid nanocomposite

Graphene oxide (GO)/ZnO nanoparticles were fabricated using a method which is well documented by Zhong *et al.*[48] 0.5 g of ball milled ZnO nanoparticles were dispersed in 10 mL of dimethyl sulfoxide (DMSO) and ultrasonicated for 2.5 h. Then 10 mL of 3-aminopropyltriethoxysilane (APTS) was added to the solution and ultrasonicated for another 2.5 h. After that, the solution was centrifuged at 4500 rpm for 15 min to separate ZnO–APTS nanoparticles. The nanoparticles were washed 3 times with ethanol and dried at 60 °C in an oven overnight. 0.04 g of amino functionalized ZnO nanoparticles and 0.04 g of GO were dispersed in 60 mL of dimethylformamide (DMF) *via* ultrasonication for 5 h, and then the solution was rested for 1 h to precipitate unattached ZnO nanoparticles. GO/ZnO

solution in DMF was centrifuged at 4500 rpm for 2.5 h. The precipitated GO/ZnO nanocomposite was washed with ethanol and centrifuged at 4500 rpm for 10 min, and the ethanol supernatant was removed 3 times and finally dried at 35 °C under vacuum overnight.

2.4 Reduction of the GO/ZnO hybrid nanocomposite with ascorbic acid

To reduce the GO/ZnO nanocomposite to rGO/ZnO according to Abulizi et al.,[39] 0.04 g of the GO/ZnO hybrid nanocomposite was dispersed in 400 mL of DI water and ultrasonicated for 1 h. 0.4 g of ascorbic acid was added to 400 mL of an aqueous dispersion of GO/ZnO and stirred vigorously for 15 min. In order to get colloidal stability by the electrostatic repulsion, the pH of the solution was adjusted to 10 using a 3 M NH_4OH solution. Then the solution was stirred at 70 °C for 3 h to get the rGO/ZnO hybrid composite. The solution was centrifuged at 10^4 rpm for 2 h, and then the supernatant was removed and washed with DI water. This process was repeated 3 times to remove unreacted materials from the rGO/ZnO hybrid nanocomposite.

2.5 Electrochemical tests and supercapacitor design

The electrochemical behavior of the electrode materials in a 6 M KOH electrolyte was characterized with a BioLogic VMP 300 multipotentiostat by using the standard two-electrode technique. Electrochemical properties and supercapacitor performances were examined by employing different electrochemical methods including cyclic voltammetry (CV), potentiostatic electrochemical impedance spectroscopy (PEIS) and galvanostatic cycling with potential limitation (GCPL). CV curves were recorded within a voltage range of 0 to +1 V at various scan rates from 5 to 200 mV s^{-1}. PEIS was carried out by applying a sinusoidal signal of 10 mV from 10 mHz to 1 MHz frequency. GCPL measurements were performed at room temperature and at various specific currents of 0.10, 0.15, 0.20, 0.30, 0.50 and 2.40 A g^{-1} in the voltage range between 0 and +1 V. All-in-one supercapacitor devices were designed in four different asymmetric configurations using electrode materials of rGO/ZnO nanocomposites or ZnO at one side and rGO at the other side, as listed in Table 1, all in the form of a powder with no binder or additive.

2.6 Characterization methods

X-ray diffraction (XRD) patterns were obtained to characterize the phase composition and crystal structure of the synthesized materials using a Bruker, D2 Phaser with a Cu-Kα radiation wavelength of 1.5418 Å, and voltage and current values of 40 kV and 40 mA, respectively. The measurements were performed at a range of 2θ = 10–90° and a step size of 0.02°. ZnO nanoparticles, GO/ZnO and rGO/ZnO were imaged using a field emission scanning electron microscope (Zeiss, SUPRA VP 35) at a 4 kV accelerating voltage. Energy dispersive X-ray (EDX) analysis was performed to determine the attached ZnO nanoparticles on the surface of GO and rGO at a 10 kV accelerating voltage and an 8.5 mm working distance. Raman measurements were performed with a high resolution inVia Raman Microscope (Renishaw inVia, excited at 532 nm) on graphite, GO, rGO, GO/ZnO and rGO/ZnO.

X-Band (9.65 GHz) EPR measurements were performed in two of the HEBM samples of ZnO, rGO, and rGO/ZnO. We used a rectangular TE102 resonator of a Bruker EMX spectrometer. The offset in the magnetic field and the exact g-factors in X-band measurements were determined with a polycrystalline DPPH (2-diphenyl-1-picrylhydrazyl) reference sample with a well-known g-factor (g = 2.0036). The EPR spectral analysis has been performed using the WINEPR program from Bruker. The following EPR experimental parameters were used: microwave power: 2 mW; modulation amplitude: 1 G; time constant: 163.84 ms; and receiver gain: 2×10^4.

3. Results and discussion

The formation of graphene sheets was verified by X-ray diffraction of the starting and synthesized materials (Fig. 1). Graphite has a sharp peak around 26.5° corresponding to the basal reflection (002) peak with the intercellular spacing in the crystal d = 0.336 nm. Graphene oxide shows a broad peak around 2θ = 11° with the spacing between the planes d = 0.81 nm indicating the (001) diffraction peak of graphite oxide. The increase in distance between the planes is attributed to the formation of oxygen containing functional groups and inserted water molecules between the carbon layers. The broad peak with low intensity in the range of 17–24° with a d-spacing of 0.37 nm means that graphene oxide is not fully interconnected with oxygen atoms.[49,50] Reduction with ascorbic acid caused the peak at 11° to vanish and a broad weak peak at 24° indicates the distorted graphite structure and hence suggests the formation of graphene sheets.[51,52]

Raman spectroscopy was used to investigate the evolution of the defects in as-received and synthesized powders (Fig. 2). On comparing the Raman spectra of three samples, notable differences are observed between them. The spectra of graphite

Table 1 Selected materials as cell components for the assembly of all-in-one supercapacitor devices

Design number	Electrode material 1 (E1)	Electrode material 2 (E2)	Electrolyte (El)	Separator (S)	Type
D1	15 min HEBM ZnO	rGO	6 M KOH	Glass fiber	Asymmetric
D2	10 h HEBM ZnO	rGO	6 M KOH	Glass fiber	Asymmetric
D3	15 min HEBM rGO/ZnO nanocomposite	rGO	6 M KOH	Glass fiber	Asymmetric
D4	10 h HEBM rGO/ZnO nanocomposite	rGO	6 M KOH	Glass fiber	Asymmetric

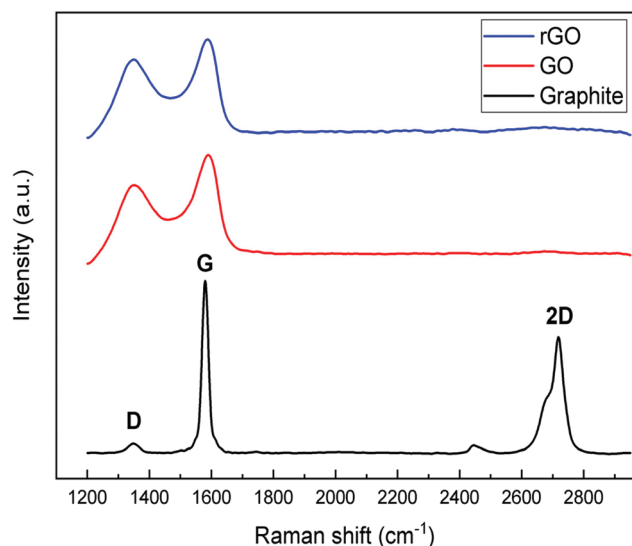**Fig. 1** XRD patterns of graphite, GO and rGO.

Fig. 2 Raman spectra of graphite, GO and rGO.

carbon sheets is due to the strong oxidative treatment of graphite. In the Raman spectra of GO, the G band is shifted from 1580 cm^{-1} to 1592 cm^{-1}, which confirmed that the individual layer reduces during the oxidation process. After the reduction of GO (GO→rGO), the D band is broadened and shifted to around 1325 cm^{-1} due to the reduction in the size of the in-plane sp^2 domains due to extensive oxidation.[53]

In Fig. 3, the XRD patterns of high-energy ball milled ZnO and rGO/ZnO are shown. The patterns show pure ZnO with a hexagonal crystalline structure with main peaks at 31.74°, 34.41° and 36.23° which are in good agreement with the JCPDS file or ICDDPDF code: 36-1451. Moreover, the crystallinity degree and crystallite size were changed by changing the ball mill time in comparison with the ZnO bulk sample. The broadening of the XRD pattern with increasing ball milling time is because of the reduction in the average particle and crystallite size and the strain induced mechanical deformation during the ball milling process.[54,55] The particle size was calculated using the Scherrer[56] equation which is 500 nm, 55 nm and 15 nm for bulk, 15 minutes and 10 hours ball milled samples, respectively. Interestingly, even 15 minutes of ball milling has a significant effect on the ZnO particle size and reduces the particle size nearly 10 times. rGO/ZnO samples show similar peaks related to ZnO nanoparticles.

Fig. 3 XRD patterns of bulk and ball milled ZnO nanoparticles as well as the rGO and ZnO hybrid composite materials.

show three characteristic bands, which are 2D, G, and D, located around 2718 cm^{-1}, 1580 cm^{-1} and 1349 cm^{-1}, respectively. The relatively low D band which is related to disorder implies that the defects on graphite might be negligible. On the other hand, a strong D band appears in both spectra of GO and rGO, which means that disorder in the sp^2 hybridized

Fig. 4 SEM images of bulk and ball milled ZnO and rGO–ZnO composites.

SEM images of ZnO nanoparticles and rGO/ZnO hybrid nanocomposites at different ball milling times are shown in Fig. 4. As shown in the pictures, on increasing the ball milling time, the particle size decreases and hexagonal crystals of ZnO suffer deformation because of the strain induced in ball milling. These results are in good agreement with the XRD

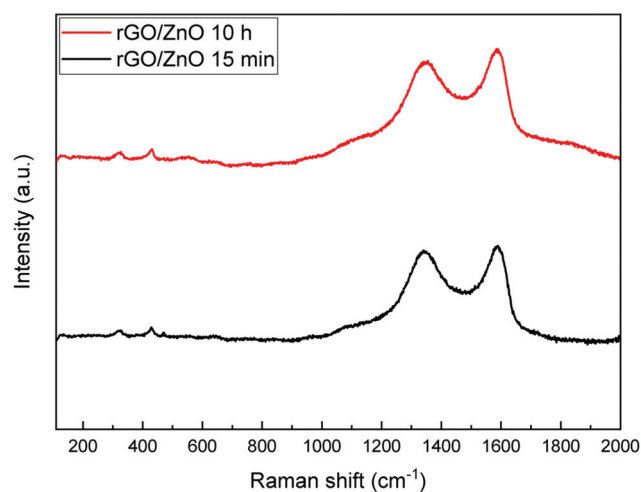**Fig. 5** EDX results of the rGO/ZnO hybrid composite.

Fig. 6 Raman spectra of the rGO/ZnO hybrid composite. Left peak: D-band and right peak: G-band.

results in Fig. 3. Moreover, the picture shows ZnO nanoparticles attached to the surface of rGO as the rGO/ZnO hybrid nanocomposite.

In Fig. 5, normalized EDX results prove the presence of carbon, oxygen and zinc in the rGO/ZnO hybrid nanocomposite. The nitrogen peak originating from APTS is used to attach ZnO nanoparticles onto the surface of GO. Moreover, on increasing the ball milling time, the intensity of Zn decreased while the intensity of oxygen increased, indicating an increase in Zn vacancies and oxygen interstitials.

Fig. 6 shows the Raman spectra of the fabricated rGO/ZnO hybrid nanocomposite. The band around 329 cm^{-1} is attributed to the second-order Raman spectrum arising from zone-boundary phonons of hexagonal ZnO. The band near 430 cm^{-1} is due to the vibration of the O sublattice, indicating the non-polar optical phonon E_2 (high) vibration mode of ZnO
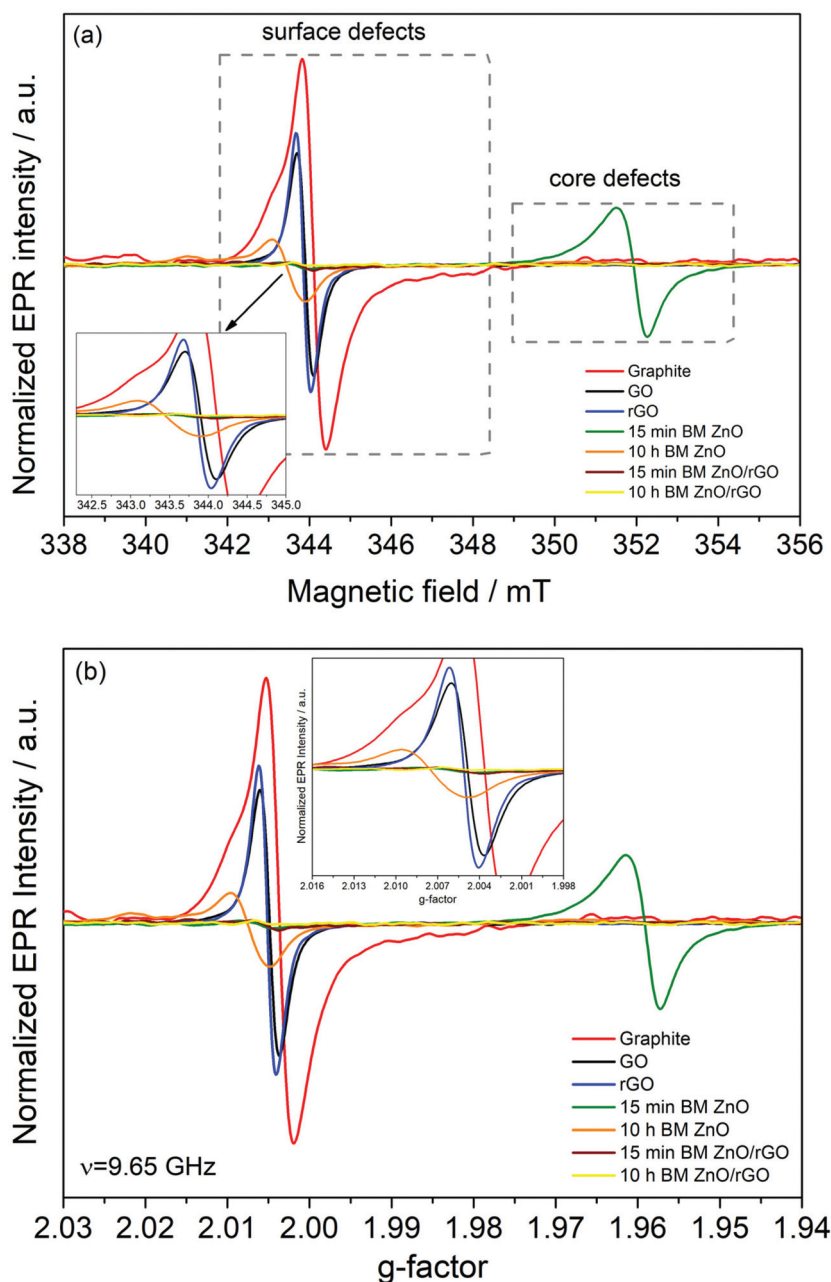

Fig. 7 Room temperature X-band EPR spectra (a) and corresponding g-values (b) of the starting materials and the synthesized powders for super-capacitor electrodes. The EPR intensities are normalized according to the mass of each sample. All EPR measurements were performed under the same conditions with the same parameters (i.e., the same receiver gain, scan number, modulation frequency, modulation amplitude, time constant and microwave power).

in the wurtzite structure.[57,58] Moreover, the bands around 1345 cm^{-1} and 1590 cm^{-1} correspond to the D and G bands. The D band is formed because of the defects created by the oxygen containing functional groups on the graphene's basal plane and the G band originates from the first-order scattering of the E$_{2g}$ mode.[59] Thus, the Raman spectra of rGO/ZnO show characteristic bands of ZnO and rGO together.

The presence of surface and core defects in the ball milled ZnO samples was investigated using X-band EPR. Fig. 7a shows the comparison of the EPR results for 15 min and 10 h HEBM ZnO. These data revealed significant results, in line with the literature that is a combination of previous PL, Raman and electrical results; the surface defects play a major role in the enhancement of electrochemical performance (see the below section) while the concentration of surface defects in 10 h HEBM ZnO is much higher compared to that of 15 min HEBM ZnO. A g-factor of ~2.004, which is very close to the g-factor of a free electron (g_e = 2.0023), was measured for both starting materials and the electrode materials ball milled for different times, indicating a free electron spin behavior due to atomic vacancies (Fig. 7b). Based on our experiments on the electrochemical performances of the supercapacitors made of these electrode materials (see the following section), these defects are found to contribute to the conduction process at room temperature.

The EPR data confirm that the number of both surface and core defects reduced in the rGO containing nanocomposites compared to those of the starting materials and HEBM ZnO nanoparticles. Also, the presence of rGO with surface defects enhanced the conductivity of the rGO/ZnO nanocomposites. That is, the critical properties, such as electrical conductivity and the number and type of defects, have been successfully tailored *via* both reduction of GO to rGO and by the controlled milling time.

3.1 Supercapacitor performance tests

To evaluate the electrochemical performance of ZnO and rGO/ZnO nanocomposites high-energy ball milled for 15 min and 10 h, GCPL, CV and PEIS were performed using a two-electrode electrochemical cell in 6 M KOH. The Nyquist and Bode plots of the four capacitors in the frequency range of 10 mHz to 1 MHz are presented in Fig. 8, respectively. In Fig. 8a, the top inset shows the experimental data at high frequencies and the bottom inset shows the equivalent circuit used for fitting the experimental data. The intercepts of the curves with the x-axis (with the real part of the impedance at a high-frequency region) represent the equivalent series resistance (R_S) which includes the resistance of the electrolyte, the contact resistance at the interface between the electrode and the current collector and the resistance of the active material. The R_S values of 0.206, 0.224, 0.178 and 0.471 Ω were obtained for the designs of D1, D2, D3 and D4, respectively, indicating low contact resistances and improved ion transfer from the electrolyte. The lower R_S value and the steeper Warburg slope of D3 than those of the other asymmetric supercapacitors suggest that the incorporation of ZnO that is rich in core defects improved the charge transfer performance and ion diffusion of the rGO electrode. Moreover, no semicircle was observed in the high frequency region in any of the Nyquist plots, indicating the fast charge transfer processes (or low contact resistance) and the pseudocapacitance arising from the redox reactions at the electrode/electrolyte interfaces. The constant phase element (Q) in the equivalent circuit is to represent the deviation from the ideal capacitance and diffusion behavior due to the non-homogeneity of the surface at the electrode–electrolyte interface. Fig. 8b shows the Bode magnitude and phase angle plots with respect to the log of the frequency on the x-axis. The frequency dependence of the impedance and phase angle for all devices are similar. That is, the impedance decreases as the frequency increases, which is a typical capacitive behavior, and then, slightly increases at higher frequencies most probably due to series resistance. A similar trend was also observed for the phase angle, confirming that the capacitive behavior is dominant at higher frequencies.

Fig. 9a shows the CV profiles of D1, D2, D3 and D4 at a scan rate of 100 mV s^{-1} in an aqueous 6 M KOH electrolyte. The CV profiles exhibit an almost conical-tapered shape slightly deviating from the rectangular shape, reflecting both the pseudocapacitor and EDLC behaviors. The highest and

Fig. 8 Electrochemical impedance spectra of the asymmetric supercapacitors D1, D2, D3 and D4 with a 6 M KOH electrolyte. (a) Nyquist plot (top inset: high frequency region and bottom inset: equivalent circuit used to fit the experimental data) and (b) Bode plot.

Fig. 9 Electrochemical performances of supercapacitors D1, D2, D3 and D4 with a 6 M KOH electrolyte: (a) CV taken at a 100 mV s^{-1} scan rate, (b) charge–discharge curves cycled between 0 and 1 V at a current density of 0.30 A g^{-1}, (c) specific capacitances at various current densities, and (d) comparison of the capacitance retention of D1, D2, D3 and D4.

lowest conductivities were observed for the supercapacitors D3 and D4, respectively. The highest discharge capacity of 0.032 mA h g^{-1} at the 10th discharge was obtained for D4 from the potential *versus* specific capacity profiles at a current density of 0.30 A g^{-1} (Fig. 9b). It was shown that all the electrodes stabilize their performances upon the first few cycles (Fig. 9c). The capacitance retention percentages of all devices increase with the increasing number of cycles and they exhibit outstanding cycling stability with a capacitance retention of 100% after 30 cycles at 0.30 A g^{-1}. As shown in Fig. 9d, the coulombic efficiencies were 97.7%, 97.2%, 93.0% and 99.2% for D1, D2, D3 and D4, respectively.

Overall, the electrochemical performance results are quite impressive for this materials system while we do not use any additives or doping or any other functional groups which are typical foreign groups for improving the system performance. Here it has been aimed to show the electrochemical performance of the bare composite which is promising for energy storage and harvesting issues.

4. Conclusions

rGO/ZnO nanocomposites for supercapacitor applications *via* high energy ball milling and modified Hummers' method

were synthesized and a wide range of characterization techniques were employed for understanding the structural (*via* XRD) and electronic properties (*via* Raman and EPR) as well as electrochemical performance (*via* potentiostat) of the fabricated supercapacitors. The data collected using these techniques have confirmed the successful fabrication of the nanocomposites and have given analytical information regarding their defect structures. Systematically, ZnO and rGO were solely investigated and then synergistic effects were observed in the hybrid nanocomposite, rGO/ZnO. The findings of this research demonstrate that compared to individual metal oxide and rGO, the rGO/ZnO nanocomposite is a promising materials system for achieving good capacitive performance for the development of supercapacitor devices. To produce such higher performance supercapacitor devices, the defect structures in metal oxides should be controlled in an extensive way. In particular, surface defects play a major role in ZnO materials. The EPR technique enables us to separate the surface and bulk defects, whereas the HEBM technique enables us to control the concentration of defects *via* controlling the milling time. Here, 10 h ball milling revealed an enormous amount of surface defects in ZnO compared to 15 min milling time. For the rGO case, it is reversed when compared to GO and graphite; the rGO has substantially fewer defects. This is also important, showing that the system can accommo-

date more charges which results in an increase in the conductivity. This work particularly shows the interplay between the defect structures of two different materials systems and their competing effects once they have been synthesized as a nanocomposite.

Conflicts of interest

There are no conflicts to declare.

Acknowledgements

References

1 K. S. Novoselov, et al., Two-dimensional gas of massless Dirac fermions in graphene, Nature, 2005, 438(7065), 197–200.

2 G. C. Wang, et al., Synthesis of highly dispersed zinc oxide nanoparticles on carboxylic graphene for development a sensitive acetylcholinesterase biosensor, Sens. Actuators, B, 2014, 190, 730–736.

3 J. D. Qiu, J. Huang and R. P. Liang, Nanocomposite film based on graphene oxide for high performance flexible glucose biosensor, Sens. Actuators, B, 2011, 160(1), 287–294.

4 R. F. Nie, et al., Platinum supported on reduced graphene oxide as a catalyst for hydrogenation of nitroarenes, Carbon, 2012, 50(2), 586–596.

5 C. A. Ma, et al., Low loading platinum nanoparticles on reduced graphene oxide-supported tungsten carbide crystallites as a highly active electrocatalyst for methanol oxidation, Electrochim. Acta, 2013, 114, 133–141.

6 Y. C. Liu, et al., Synthesis of MnO_2/graphene/carbon nanotube nanostructured ternary composite for supercapacitor electrodes with high rate capability, Mater. Chem. Phys., 2014, 147(1–2), 141–146.

7 A. K. Mishra and S. Ramaprabhu, Functionalized Graphene-Based Nanocomposites for Supercapacitor Application, J. Phys. Chem. C, 2011, 115(29), 14006–14013.

8 J. Kim, et al., Synthesis of Li2MnSiO4-Graphene Composite and Its Electrochemical Performances as a Cathode Material for Lithium Ion Batteries, J. Nanosci. Nanotechnol., 2014, 14(10), 7898–7902.

9 S. Park and R. S. Ruoff, Chemical methods for the production of graphenes, Nat. Nanotechnol., 2009, 4(4), 217–224.

10 A. Gonzalez, et al., Review on supercapacitors: Technologies and materials, Renewable Sustainable Energy Rev., 2016, 58, 1189–1206.

11 G. Wang, L. Zhang and J. Zhang, A review of electrode materials for electrochemical supercapacitors, Chem. Soc. Rev., 2012, 41(2), 797–828.

12 A. González, et al., Review on supercapacitors: technologies and materials, Renewable Sustainable Energy Rev., 2016, 58, 1189–1206.

13 E. Edri, H. Cohen and G. Hodes, Band Alignment in Partial and Complete ZnO/ZnS/CdS/CuSCN Extremely Thin Absorber Cells: An X-ray Photoelectron Spectroscopy Study, ACS Appl. Mater. Interfaces, 2013, 5(11), 5156–5164.

14 Q. Chen, et al., Passivation of surface states in the ZnO nanowire with thermally evaporated copper phthalocyanine for hybrid photodetectors, Nanoscale, 2013, 5(10), 4162–4165.

15 G. Ouyang and G. W. Yang, ZnO Hollow Quantum Dot: A Promising Deep-UV Light Emitter, ACS Appl. Mater. Interfaces, 2012, 4(1), 210–213.

16 S. Repp and E. Erdem, Controlling the exciton energy of zinc oxide (ZnO) quantum dots by changing the confinement conditions, Spectrochim. Acta, Part A, 2016, 152, 637–644.

17 S. Parashar, et al., Investigation of intrinsic defects in core-shell structured ZnO nanocrystals, J. Appl. Phys., 2012, 111(11), 113712.

18 H. Kaftelen, et al., EPR and photoluminescence spectroscopy studies on the defect structure of ZnO nanocrystals, Phys. Rev. B: Condens. Matter Mater. Phys., 2012, 86(1), 014113.

19 E. Erdem, Microwave power, temperature, atmospheric and light dependence of intrinsic defects in ZnO nanoparticles: A study of electron paramagnetic resonance (EPR) spectroscopy, J. Alloys Compd., 2014, 605, 34–44.

20 S. Nadupalli, et al., About defect phenomena in ZnO nanocrystals, Nanoscale, 2021, 13(20), 9160–9171.

21 X. Zhao, H. Bin, et al., Preparation, characterization, and application of graphene-zinc oxide composites (G-ZnO) for the adsorption of Cu(II), Pb(II) and Cr(III), J. Chem. Eng., 2013, 58, 2395–2401.

22 J. M. Lee, et al., ZnO Nanorod-Graphene Hybrid Architectures for Multifunctional Conductors, J. Phys. Chem. C, 2009, 113(44), 19134–19138.

23 C. V. Pham, et al., Charge transfer and surface defect healing within ZnO nanoparticle decorated graphene hybrid materials, Nanoscale, 2016, 8(18), 9682–9687.

24 C. V. Pham, et al., Comparative electron paramagnetic resonance investigation of reduced graphene oxide and carbon nanotubes with different chemical functionalities for quantum dot attachment, Appl. Phys. Lett., 2014, 104(13), 132102.

25 Y. Yang and T. X. Liu, Fabrication and characterization of graphene oxide/zinc oxide nanorods hybrid, Appl. Surf. Sci., 2011, 257(21), 8950–8954.

26 M. Ahmad, E. Ahmed, A. Elhiss, Z. L. Hong and N. R. Khalid, Enhancing visible light resonsive photocatalytic activity by decorating Mn-doped ZnO nanoparticles on graphene, Ceram. Int., 2014, 40, 10085–10097.

27 G. Du, Y. Li, L. Zhang, X. Wang, P. Liu, Y. Feng and X. Sun, Facile self-assembly of honeycomb ZnO particles decorated reduced graphene oxide, *Mater. Lett.*, 2014, **128**, 242–244.

28 J. Cembrero, *et al.*, Effect of combined chemical and electrochemical reduction of graphene oxide on morphology and structure of electrodeposited ZnO, *Ceram. Int.*, 2014, **40**(7), 10351–10357.

29 S. Park, J. An, R. D. Piner, I. Jung, D. Yang, A. Velamakanni, S. T. Nguyen and R. S. Ruoff, *Chem. Mater.*, 2008, **20**, 6592.

30 D. A. Dinh, K. S. Hui, K. N. Hui, Y. R. Cho, W. Zhou and X. Hong, Green synthesis of high conductivity silver nanoparticle-reduced graphene oxide composite films, *Appl. Surf. Sci.*, 2014, **298**, 62–67.

31 Z. Yunfei, *et al.*, Improved efficiency of hybrid solar cells based on non-ligand-exchanged CdSe quantum dots and poly(3-hexylthiophene), *Appl. Phys. Lett.*, 2010, **96**(1), 013304.

32 W. Zou, J. Zhu, Y. Sun and X. Wang, Depositing ZnO nanoparticles onto graphene in a polyol system, *Mater. Chem. Phys.*, 2011, **125**, 617–620.

33 M. Y. Xing, X. Li and J. L. Zhang, Synergistic effect on the visible light activity of Ti3+ doped TiO2 nanorods/boron doped graphene composite, *Sci. Rep.*, 2014, **4**, 5493.

34 J. X. Guo, *et al.*, Monodisperse SnO2 anchored reduced graphene oxide nanocomposites as negative electrode with high rate capability and long cyclability for lithium-ion batteries, *J. Power Sources*, 2014, **262**, 15–22.

35 M. Mitra, *et al.*, Reduced graphene oxide-polyaniline composites—synthesis, characterization and optimization for thermoelectric applications, *RSC Adv.*, 2015, **5**(39), 31039–31048.

36 H. Rasouli, L. Naji and M. G. Hosseini, 3D structured polypyrrole/reduced graphene oxide (PPy/rGO)-based electrode ionic soft actuators with improved actuation performance, *New J. Chem.*, 2018, **42**(14), 12104–12118.

37 K. K. H. De Silva, H.-H. Huang and M. Yoshimura, Progress of reduction of graphene oxide by ascorbic acid, *Appl. Surf. Sci.*, 2018, **447**, 338–346.

38 Z. Khosroshahi, *et al.*, *Green reduction of graphene oxide by ascorbic acid*, in *AIP Conference Proceedings*, AIP Publishing LLC, 2018.

39 A. Abulizi, K. Okitsu and J.-J. Zhu, Ultrasonic assisted reduction of graphene oxide to graphene in L-ascorbic acid aqueous solutions: kinetics and effects of various factors on the rate of graphene formation, *Ultrason. Sonochem.*, 2014, **21**, 1174–1181.

40 A. U. Ammar, *et al.*, ZnO and MXenes as electrode materials for supercapacitor devices, *Beilstein J. Nanotechnol.*, 2021, **12**, 49–57.

41 S. Najib, *et al.*, Tailoring morphology to control defect structures in ZnO electrodes for high-performance supercapacitor devices, *Nanoscale*, 2020, **12**(30), 16162–16172.

42 M. Toufani, *et al.*, Synergy of nano-ZnO and 3D-graphene foam electrodes for asymmetric supercapacitor devices, *Nanoscale*, 2020, **12**(24), 12790–12800.

43 W. S. Hummers and R. E. Offeman, Preparation of Graphitic Oxide: Journal of the American Chemical Society, *J. Am. Chem. Soc.*, 1958, **80**(6), 1339.

44 N. I. Kovtyukhova, *et al.*, Layer-by-layer assembly of ultrathin composite films from micron-sized graphite oxide sheets and polycations, *Chem. Mater.*, 1999, **11**(3), 771–778.

45 P. Giri, *et al.*, Correlation between microstructure and optical properties of ZnO nanoparticles synthesized by ball milling, *J. Appl. Phys.*, 2007, **102**(9), 093515.

46 M. Broseghini, *et al.*, Homogeneity of ball milled ceramic powders: Effect of jar shape and milling conditions, *Data Brief*, 2017, **10**, 186–191.

47 A. Glushenkov, H.-Z. Zhang and Y. Chen, Reactive ball milling to produce nanocrystalline ZnO, *Mater. Lett.*, 2008, **62**(24), 4047–4049.

48 L. Zhong and K. Yun, Graphene oxide-modified ZnO particles: synthesis, characterization, and antibacterial properties, *Int. J. Nanomed.*, 2015, (10 Spec Iss), 79–92.

49 X. F. Gao, J. Jang and S. Nagase, Hydrazine and Thermal Reduction of Graphene Oxide: Reaction Mechanisms, Product Structures, and Reaction Design, *J. Phys. Chem. C*, 2010, **114**(2), 832–842.

50 M. C. Hsiao, *et al.*, Preparation of Covalently Functionalized Graphene Using Residual Oxygen-Containing Functional Groups, *ACS Appl. Mater. Interfaces*, 2010, **2**(11), 3092–3099.

51 K. Krishnamoorthy, *et al.*, Antibacterial Efficiency of Graphene Nanosheets against Pathogenic Bacteria via Lipid Peroxidation, *J. Phys. Chem. C*, 2012, **116**(32), 17280–17287.

52 O. C. Compton, *et al.*, Electrically Conductive "Alkylated" Graphene Paper via Chemical Reduction of Amine-Functionalized Graphene Oxide Paper, *Adv. Mater.*, 2010, **22**(8), 892–896.

53 A. C. Ferrari, *et al.*, Raman spectrum of graphene and graphene layers, *Phys. Rev. Lett.*, 2006, **97**(18), 187401.

54 L. C. Damonte, *et al.*, Nanoparticles of ZnO obtained by mechanical milling, *Powder Technol.*, 2004, **148**(1), 15–19.

55 P. K. Giri, *et al.*, Correlation between microstructure and optical properties of ZnO nanoparticles synthesized by ball milling, *J. Appl. Phys.*, 2007, **102**(9), 093515.

56 A. L. Patterson, The Scherrer Formula for X-Ray Particle Size Determination, *Phys. Rev.*, 1939, **56**(10), 978–982.

57 R. Cusco, *et al.*, Temperature dependence of raman scattering in ZnO, *Phys. Rev. B: Condens. Matter Mater. Phys.*, 2007, **75**(16), 165202.

58 R. Zhang, *et al.*, Photoluminescence and Raman scattering of ZnO nanorods, *Solid State Sci.*, 2009, **11**(4), 865–869.

59 D. Yang, *et al.*, Chemical analysis of graphene oxide films after heat and chemical treatments by X-ray photoelectron and Micro-Raman spectroscopy, *Carbon*, 2009, **47**(1), 145–152.